Influence of physical interactions on spatiotemporal patterns

Chengjie Luo [*] and David Zwicker [†]
Max Planck Institute for Dynamics and Self-Organization, Am Faßberg 17, 37077 Göttingen, Germany

(Received 26 May 2023; accepted 31 August 2023; published 18 September 2023)

Spatiotemporal patterns are often modeled using reaction-diffusion equations, which combine complex reactions between constituents with ideal diffusive motion. Such descriptions neglect physical interactions between constituents, which might affect resulting patterns. To overcome this, we study how physical interactions affect cyclic dominant reactions, like the seminal rock-paper-scissors game, which exhibits spiral waves for ideal diffusion. Generalizing diffusion to incorporate physical interactions, we find that weak interactions change the length- and time scales of spiral waves, consistent with a mapping to the complex Ginzburg-Landau equation. In contrast, strong repulsive interactions typically generate oscillating lattices, and strong attraction leads to an interplay of phase separation and chemical oscillations, like droplets co-locating with cores of spiral waves. Our work suggests that physical interactions are relevant for forming spatiotemporal patterns in nature, and it might shed light on how biodiversity is maintained in ecological settings.

DOI: 10.1103/PhysRevE.108.034206

I. INTRODUCTION

Complex spatiotemporal patterns are ubiquitous in nature. Examples on microscopic scales include the Belousov-Zhabotinsky (BZ) reaction [1], chemical waves created by amoebae [2], and electrical patterns in human hearts [3]. On larger scales, complex patterns emerge in bacterial colonies [4,5], lizard populations [6], and human society [7,8]. In all cases, patterns emerge from spatial motion and local interactions, like chemical reactions, mating, and competition. These dynamics are typically modeled as reaction-diffusion equations, where nonlinear reactions are combined with ideal diffusive motion [9]. This choice, however, implies that physical interactions that give rise to nonlinear local behavior are neglected in the spatial dynamics.

Physical interactions inevitably affect spatial dynamics. For example, the run-and-tumble motility of bacteria leads to motility-induced phase separation [10], which can be rationalized as physical interactions leading to phase separation. Works on surface chemical reactions [11–16] show that strong attractive interaction can lead to Turing-like patterns and traveling waves. Physical interactions are also responsible for spatial patterns of proteins on cell membranes, such as MinCDE in bacteria [17,18] and MARCKS in eukaryotic cells [19]. To generalize observations of these specific models, we here investigate the role of physical interactions on spatiotemporal patterns in a generic model focusing on cyclic dominant local interactions.

Cyclic dominant interactions, like the seminal rock-paper-scissors game [20–22], naturally produce temporal oscillations [23]. Combined with ideal diffusion [24] or hopping [25,26], cyclic dominant reactions produce spatiotemporal patterns. In particular, spiral waves form when the mobilities of species are low, while spatial patterns are lost for large mobilities [24,27]. Spatial patterns also often subside when random mutations are too prevalent [25,26,28,29]. Interestingly, many of these models can be reduced to the complex Ginzburg-Landau equation (CGLE), e.g., by projection onto a reactive manifold [30] or a multiscale expansion [25]. Such mappings allow us to determine parameter regions of spatiotemporal patterns, including vortices, spiral waves, and spatiotemporal chaos [31–33].

In this paper, we consider a general model of cyclic dominant reactions coupled to diffusive motion including physical interactions. In the absence of reactions, the physical interactions can lead to phase separation, where all species co-segregate from the inert solvent (for strong attraction) or all segregate from each other (for strong repulsion). We recently analyzed the effect of such interactions on static Turing patterns and found that even weak interactions, which would not lead to phase separation by themselves, can strongly affect the resulting patterns [34]. While we here identify similar behavior for cyclic dependent reactions, we also discover entirely new spatiotemporal patterns for strong interactions. To introduce all these effects in detail, the paper is organized as follows: We introduce the model in Sec. II A, identify six relevant parameter regions using linear stability analysis in Sec. II B, and then discuss these regions in detail using numerical simulations and more detailed analysis in the subsequent sections.

[*] chengjie.luo@ds.mpg.de
[†] david.zwicker@ds.mpg.de

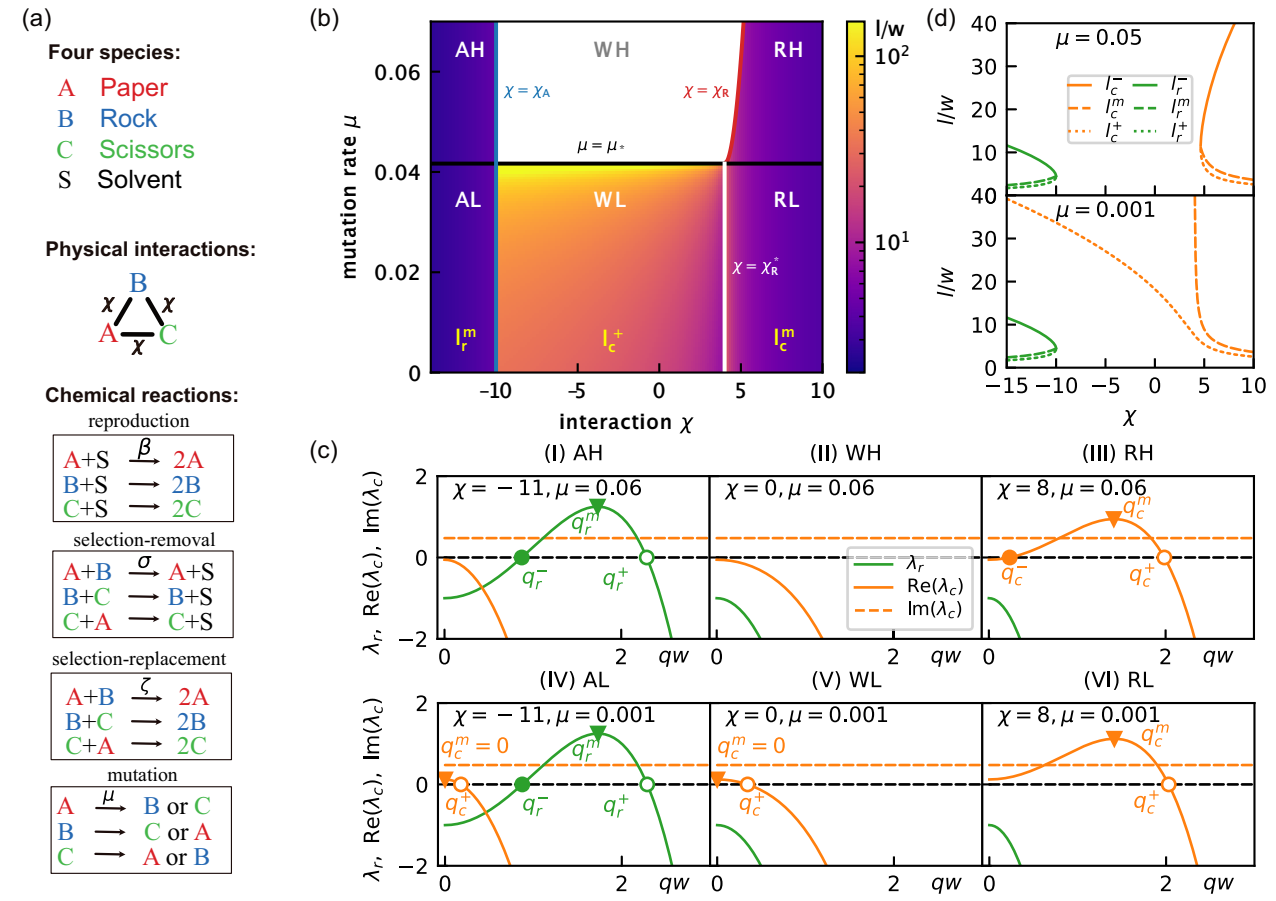

FIG. 1. Linear stability analysis reveals distinct parameter regions. (a) Schematic of physical interactions and chemical reactions of three species A, B, C, and the inert solvent S. (b) Stability diagram distinguishing regions of low (L) and high (H) mutation rate μ as well as strong attraction (A), weak interaction (W), and strong repulsion (R). The critical lines follow from Eq. (4) (black line), Eq. (9a) (blue line), Eq. (9b) (red line), and $\chi_R^{eq} = 1/\phi_0$ (white line). The colors represent the length scales l_r^m in regimes AH and AL, l_c^m in RH and RL, and l_c^+ in WL. (c) Representative dispersion relations $\lambda(q)$ in the six regimes. Green curves represent real eigenvalues $\lambda_r(q)$ with left root (q_r^-, green disk), right root (q_r^+, green circle), and maximum (q_r^m, green triangle) marked. Solid orange curves and symbols represent the respective values for the real part of the complex eigenvalues, whereas the dashed orange lines mark the imaginary part $\mathrm{Im}(\lambda_c) = \omega_*$; see Eq. (5). (d) Typical length scales as a function of χ at $\mu = 0.05 > \mu_*$ (upper panel) and $\mu = 0.001 < \mu_*$ (lower panel). The subscript and superscript of the length scale l correspond to those of wave number q in panel (c) using $l = 2\pi/q$. (b)–(d) Additional model parameters are $\beta = \sigma = D = 1$ and $\zeta = 0.6$.

II. RESULTS

A. Model with physical and chemical interactions

We consider an incompressible, isothermal fluid comprising three species A (paper), B (rock), and C (scissors) as well as an inert solvent S. This system is described by the volume fractions $\phi_A(\boldsymbol{r}, t)$, $\phi_B(\boldsymbol{r}, t)$, and $\phi_C(\boldsymbol{r}, t)$, where $\boldsymbol{r}$ is the spatial position and t is time, and the solvent occupies the remaining fraction $\phi_S = 1 - (\phi_A + \phi_B + \phi_C)$. We explicitly include physical interactions and chemical reactions among the species in our model; see Fig. 1(a).

1. Physical interactions

We describe physical interactions using thermodynamics based on the Flory-Huggins free energy [35–37],

$$F[\phi_A, \phi_B, \phi_C] = \frac{k_B T}{\nu} \int \left[\chi(\phi_A\phi_B + \phi_A\phi_C + \phi_B\phi_C) + \sum_{i=A,B,C,S} \phi_i \ln \phi_i + \frac{1}{2} w^2 \sum_{j=A,B,C} |\nabla \phi_j|^2 \right] \mathrm{d}\boldsymbol{r}, \tag{1}$$

where the integral is over the volume of the system, $k_B T$ is the relevant energy scale, and ν denotes the molecular volume, which is the same for all species for simplicity. The first term in the square bracket describes the physical interactions among the species A, B, and C, the second term captures translational entropies of all four species, and the last term

limits the width of interfaces between coexisting phases to roughly w in strongly interacting systems [37]. The physical interactions are quantified by the Flory parameter χ: Positive χ denotes repulsion, whereas negative χ represents attraction. For simplicity, we only consider symmetric interactions, i.e., the same value of χ for all pairs of A, B, and C, while the solvent is inert, but in general the value could be species-dependent.

The free energy defined in Eq. (1) allows for inhomogeneous equilibrium states when the physical interactions are sufficiently strong [37–39]. In particular, a phase enriched in species A, B, and C segregates from the solvent S for strong attraction ($\chi < \chi_{\mathrm{A}}^{\mathrm{eq}}$), whereas strong repulsion ($\chi > \chi_{\mathrm{R}}^{\mathrm{eq}}$) leads to three phases which are each enriched in one of the species and the solvent. In the case where the species A, B, and C have equal average fraction ϕ_0, the critical values are

$$\chi_{\mathrm{A}}^{\mathrm{eq}} = -\frac{1}{2\phi_0(1-3\phi_0)} \text{ and } \chi_{\mathrm{R}}^{\mathrm{eq}} = \frac{1}{\phi_0}, \tag{2}$$

which follows from a linear stability analysis shown in the Supplemental Material [46]. Taken together, we expect that the two critical values given in Eq. (2) separate three qualitatively different regions in parameter space.

2. Cyclic dominant chemical reactions

Following previous studies of the rock-paper-scissors game [25,26], we consider general chemical reactions that include reproduction, selection, and mutation; see Fig. 1(a). Reproduction happens with rate β when a species $i \in \{A, B, C\}$ meets solvent, which could also play a role similar to empty space. Selection comes in two variants, which both encode the typical rock-paper-scissors rules, where species i dominates species $i+1$ while being dominated by species $i-1$, using the cyclically ordered index such that $A+1=B$, $B+1=C$, and $C+1=A$. The first selection variant removes the dominated species with rate σ, whereas the second variant replaces the dominated species by the dominating one with rate ζ in a zero-sum process. Finally, random mutations happen with rate μ. Combining all these processes, the reaction rate of species i reads

$$\begin{aligned} R_i = \phi_i[\beta\phi_S - \sigma\phi_{i-1} + \zeta(\phi_{i+1} - \phi_{i-1})] \\ + \mu(\phi_{i-1} + \phi_{i+1} - 2\phi_i) \end{aligned} \tag{3}$$

for $i \in \{A, B, C\}$ with positive rates β, σ, ζ, and μ. For $\beta = \sigma = \mu = 0$, the model reduces to the cyclic Lotka-Volterra model with equal replacement rate ζ [23,40], whereas $\zeta = \mu = 0$ leads to the May-Leonard model [41].

In the simplest case without spatial dependence the dynamics of the three species are given by $\partial_t\phi_i = R_i$. This system undergoes a supercritical Hopf bifurcation when μ decreases below μ_*, where [42]

$$\mu_* = \frac{\beta\sigma}{6(3\beta+\sigma)}, \tag{4}$$

and develops a stable limit cycle with frequency

$$\omega_* = \frac{\sqrt{3}\beta(2\zeta+\sigma)}{2(3\beta+\sigma)}. \tag{5}$$

Combining these oscillating reactions with ideal diffusion then leads to steady spiral waves and other oscillating states [25,26,28,29]. However, it is unclear how physical interactions affect the oscillating states and how the chemical reactions modify the equilibrium behavior of phase separation.

3. Combined model

To combine physical interactions and chemical reactions, we use the exchange chemical potentials

$$\bar{\mu}_i = \frac{\nu}{k_{\mathrm{B}}T}\frac{\delta F}{\delta\phi_i}, \tag{6}$$

to express diffusive fluxes $\boldsymbol{j}_i = -\Lambda_i\nabla\bar{\mu}_i$ in the continuity equation $\partial_t\phi_i = \nabla\cdot\boldsymbol{j}_i + R_i$ [43,44]. Hence,

$$\partial_t\phi_i = \nabla\cdot[D_i\phi_i\nabla\bar{\mu}_i] + R_i, \tag{7}$$

where R_i is given by Eq. (3). Here, D_i are the diffusivities of the species $i = A, B, C$, which are related to mobilities $\Lambda_i = D_i\phi_i$ in this multicomponent system [45].

To analyze the behavior of Eq. (7), we first use linear stability analysis to identify qualitatively different regimes and associated length scales of patterns. We then study the dynamical behavior in detail using numerical simulations in a two-dimensional system with periodic boundary conditions. In the simulations, we choose $\beta = 1$ to set the time scale, and $w = 1$ to set the length scale. For simplicity, we also set $D_i = D = 1$ for all three species to focus on how the physical interaction parameter χ, the mutation rate μ, and replacement rate ζ affect the pattern formation and cyclic behavior of the system.

B. Linear stability analysis reveals phase diagram

To reveal the basic behavior of the model, we first analyze the stability of the only uniform steady state of Eq. (7), which is $\phi_i(\boldsymbol{r}) = \phi_0$ with

$$\phi_0 = \frac{\beta}{3\beta+\sigma}. \tag{8}$$

We focus on the case of an equal average fraction $\phi_0 = \frac{1}{4}$ for A, B, C, and S, implying $\sigma = \beta$. In the linear regime of small perturbations, we assess the stability of this homogeneous state by evaluating the growth rates λ of harmonic perturbations with wave number q; see the Supplemental Material [46]. For each q, we obtain three eigenvalues of the Jacobian matrix associated with Eq. (7), of which one is always real (denoted by λ_{r}), whereas the remaining two eigenvalues are complex conjugates of each other, denoted as $\mathrm{Re}(\lambda_{\mathrm{c}}) \pm \mathrm{Im}(\lambda_{\mathrm{c}})$. The homogeneous state is unstable if any eigenvalue has a positive real part and the associated imaginary part represents the oscillation frequency, which is related to ω_* given by Eq. (5). Note that λ_{r} is independent of the mutation rate μ, whereas the stability of the complex modes depends on μ. In particular, they are stable in the limit of long wavelengths, $\mathrm{Re}(\lambda_{\mathrm{c}}(q=0)) < 0$, if and only if the mutation rate μ is higher than the critical value μ_* given by Eq. (4), which clearly distinguishes a regime of low and high mutation rate, which we denote by L and H,

respectively. Within each region, we can furthermore distinguish regions of strong attraction (region A), weak interaction (region W), and strong repulsion (region R), based on the critical values suggested by Eq. (2). The combination of these two characteristics leads to the six distinct parameter regimes shown in Fig. 1, which we will now discuss in more detail.

In region WH with *weak* interactions ($\chi_A < \chi < \chi_R$) and *high* mutation rates ($\mu > \mu_*$), the uniform solution Eq. (8) is stable, since the real parts of all eigenvalues are negative; see Fig. 1(c)(II). The critical values for the physical interactions,

$$\chi_A = \chi_A^{eq} - w\sqrt{\frac{3\beta+\sigma}{D}} \quad \text{and} \tag{9a}$$

$$\chi_R(\mu) = \chi_R^{eq} + w\sqrt{\frac{2\sigma(\mu/\mu_*-1)}{D}}, \tag{9b}$$

follow from solving $\max(\lambda_r) = 0$ and $\max(\mathrm{Re}(\lambda_c)) = 0$ for χ, respectively. Here, we used Eq. (8) to compare with χ_A^{eq} and χ_R^{eq} given by Eq. (2), which mark the influence of phase separation. Consequently, chemical reactions shift both critical values to stronger interactions, consistent with reactions suppressing phase separation [47].

In region AH with strong *attraction* ($\chi < \chi_A$) and *high* mutation rate ($\mu > \mu_*$), the real eigenvalue λ_r is positive if $q_r^- < q < q_r^+$, where q_r^- (q_r^+) is the left (right) root of λ_r; see Fig. 1(c)(I). The wavelength $l_r^m = 2\pi/q_r^m$ of the corresponding instability can be estimated from the wave number q_r^m of the most unstable mode and reads

$$l_r^m = 2\pi w\left[-\frac{2\beta\sigma}{2\beta\sigma\chi + (3\beta+\sigma)^2}\right]^{\frac{1}{2}}. \tag{10}$$

Consequently, l_r^m decreases slightly for smaller physical interaction χ; see the dashed green curve in the upper panel of Fig. 1(d). We thus expect stationary patterns with length scales close to l_r^m in region AH.

In region RH with strong *repulsion* ($\chi > \chi_R$) and *high* mutation ($\mu > \mu_*$), the complex eigenvalues λ_c exhibit an instability for $q_c^- < q < q_c^+$; see Fig. 1(c)(III). The associated most unstable wavelength $l_c^m = 2\pi/q_c^m$ reads

$$l_c^m = 2\pi w\left[\frac{2}{\chi - (3+\sigma/\beta)}\right]^{\frac{1}{2}}, \tag{11}$$

and decreases for stronger repulsion; see the dashed orange curve in the upper panel of Fig. 1(d). Since the imaginary parts for these modes are nonzero, we expect oscillating patterns with length scales close to l_c^m.

In region AL with strong *attraction* ($\chi < \chi_A$) and *low* mutation rate ($\mu < \mu_*$), we find the same unstable real modes as in region AH as well as additional unstable complex modes for $0 < q < q_c^+$, although their maximal growth rate is typically smaller than that of the real modes. However, linear stability analysis does not provide any information on how these modes interact and we thus expect a rich behavior in this region.

In region WL with *weak* interaction ($\chi_A < \chi < \chi_R$) and *low* mutation rate ($\mu < \mu_*$), the oscillating modes are unstable for $q < q_c^+$, whereas $\lambda_r < 0$; see Fig. 1(c)(V). The length scale of the most unstable mode diverges ($q_c^m = 0$), so the length scale $l_c^+ = 2\pi/q_c^+$ associated with the largest unstable wave number q_c^+,

$$l_c^+ = 2\pi w\left(\frac{2}{\tilde{\chi} + \left[\tilde{\chi}^2 + \frac{2\sigma w^2}{D}\left(1-\frac{\mu}{\mu_*}\right)\right]^{1/2}}\right)^{\frac{1}{2}}, \tag{12}$$

with $\tilde{\chi} = \chi - 3 - \sigma/\beta$, is most relevant. This length scale decreases significantly as χ increases; see dotted orange line in lower panel of Fig. 1(d).

Finally, in region RL with strong *repulsion* ($\chi > \chi_R$) and *low* mutation rate ($\mu < \mu_*$), we find the same unstable modes as in region WL, but the length scale $l_c^m = 2\pi/q_c^m$ of the most unstable mode is now finite. This length scale decreases for larger interaction parameters χ; see dashed orange curve in lower panel of Fig. 1(d). We distinguish the regions WL and RL based on whether q_c^m is zero or not, which provides the critical physical interaction $\chi_R^* = \phi_0^{-1}$. The fact that this threshold value is identical to χ_R^{eq} given by Eq. (2) suggests that the transition is governed by phase separation induced by the physical interactions.

Taken together, linear stability analysis provides a qualitative picture of the five unstable regimes, and it predicts the associated critical curves; see Fig. 1(b). The analysis also provides typical length scales in different regimes; see color shading in Figs. 1(b) and 1(d). We next corroborate the phase diagram with detailed simulations and analyze the nonlinear behavior of the model. For simplicity, we consider two-dimensional simulations in square boxes of side length L with periodic boundary conditions and we implement the spatial derivatives using finite differences [48]. The simulation results summarized in Fig. 2 indicate that the uniform state is indeed stable in region WH (black stars), whereas complex patterns emerge in the unstable regimes, which we discuss in detail in the following sections.

C. Weak interactions affect length scales but not frequency of spiral waves

We start by discussing weak physical interactions, where we expect qualitatively similar behavior to systems without interactions. In the region WL with low mutation rates, where patterns actually form, we observe two main types of oscillating patterns: Homogeneous oscillations (white squares in upper left part of region WL in Fig. 2) or spiral waves (green squares in lower right part of the region WL), which are expected from the linear stability analysis. This raises the question of why spiral waves are apparently suppressed for parameters above the diagonal green dashed line in Fig. 2.

To address this question, we first carefully analyze the regime with spiral waves. We quantify the wavelength of the spiral waves using the static spatial correlation function $g_{\alpha\beta}(r) \equiv g_{\alpha\beta}(|\mathbf{r}-\mathbf{r}'|) = \langle\phi_\alpha(\mathbf{r})\phi_\beta(\mathbf{r}')\rangle - \langle\phi_\alpha(\mathbf{r})\rangle\langle\phi_\beta(\mathbf{r}')\rangle$ from simulated snapshots. Figure 3(a) shows the cross correlation between A and B, allowing us to define the correlation length l_{corr} as the position of the first peak of g_{AB}. Figures 3(b) and 3(c) show that l_{corr} generally decreases with increasing interaction parameter χ for $\chi_A < \chi < \chi_R^*$, implying that stronger repulsion between species shortens the length scales of spiral waves.

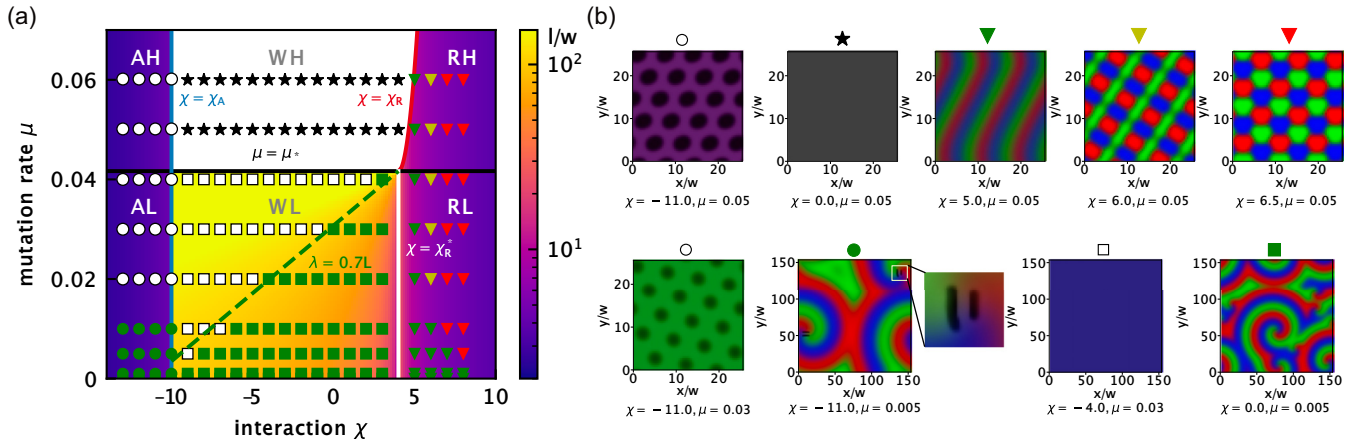

FIG. 2. Numerical simulations reveal diverse patterns. (a) Phase diagram with stability lines copied from Fig. 1(b). Background colors also correspond to Fig. 1(b), except in region WL, where they mark the length scale λ given by Eq. (13). The green dashed lines corresponds to $\lambda \approx 0.7\,L$, which fits the transition best. Symbols classify different patterns corresponding to examples in panel (b). (b) Snapshots of representative patterns for panel (a). Colors represent the abundance of the three species using RGB triplets: (red, green, blue) = (ϕ_A, ϕ_B, ϕ_C). We used $L = 25.6\,w$, $\Delta x = 0.4\,w$, and $t = 10^5\beta$ for the snapshots in the first row and the one marked with white circle in the second row. Movies of these states are enclosed with the Supplemental Material [46]. (a)–(b) Model parameters are $D = \beta = \alpha = 1$ and $\zeta = 0.6$. Simulation parameters are $L/w = 153.6$ with discretization $\Delta x/w = 0.6$ and we evaluate patterns after time $t = 10^4\beta$.

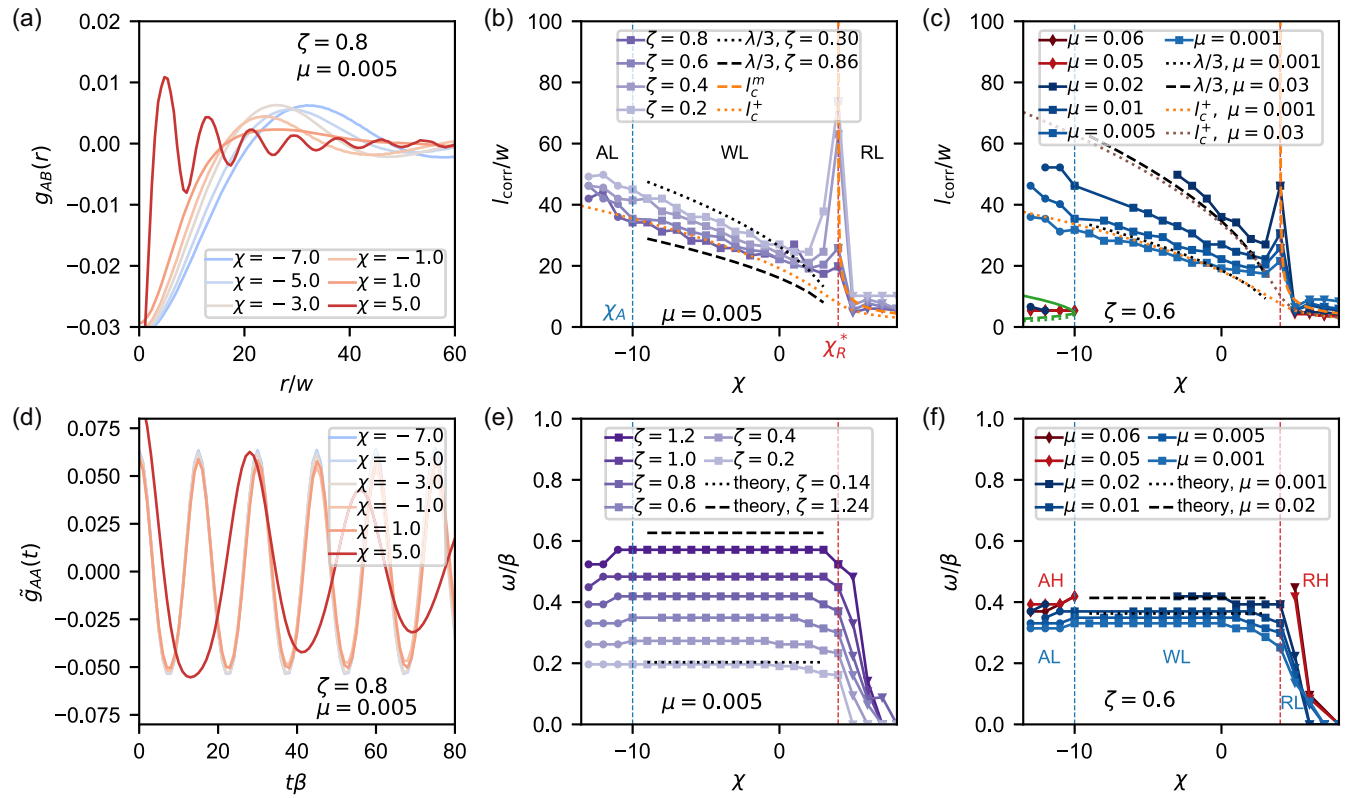

FIG. 3. Length- and time scales of dynamic patterns. (a) Spatial correlation function $g_{AB}(r)$ as a function of distance r for various physical interactions χ at $\zeta = 0.8$ and $\mu = 0.005$. (b) Correlation length scale $l_{\rm corr}$ determined from first maximum of $g_{AB}(r)$ as a function of χ at $\mu = 0.005$. The black dashed (dotted) line corresponds to $\frac{1}{3}\lambda$ calculated from Eq. (13) at $\zeta = 0.86$ ($\zeta = 0.30$). The orange lines are the same as in Fig. 1(d) at $\mu = 0.005$. (c) $l_{\rm corr}$ as function of χ for $\zeta = 0.6$. The black dashed (dotted) line corresponds to $\frac{1}{3}\lambda$ calculated by Eq. (13) at $\mu = 0.03$ ($\mu = 0.001$). The green and orange lines are the same as in Fig. 1(d) at $\mu = 0.001$. The brown dotted line is l_c^+ at $\mu = 0.03$. (d) Temporal correlation function $\tilde{g}_{AA}(t)$ as a function of lag time t for various χ at $\zeta = 0.8$ and $\mu = 0.005$. (e) Frequency ω determined from the first maximum of $\tilde{g}_{AA}$ as a function of χ for $\mu = 0.005$. The black dashed (dotted) line shows ω given by Eq. (14) for $\zeta = 1.24$ ($\zeta = 0.14$). (f) ω as a function of χ for $\zeta = 0.6$. The black dashed (dotted) line shows ω given by Eq. (14) at $\mu = 0.02$ ($\mu = 0.001$). (a)–(f) The vertical dashed blue (red) lines denote the critical interactions $\chi_{\rm A} = -10$ ($\chi_{\rm R}^* = 4$). Additional model parameters are $\beta = \alpha = D = 1$.

To understand the effect of physical interaction on spiral waves, we next use a multiscale expansion around the Hopf bifurcation $\mu = \mu_*$, to map Eq. (7) to a complex Ginzburg-Landau equation (CGLE) [25]; see Supplemental Material [46]. Note that we use identical diffusion constants for all species, so the diffusion coefficient of the CGLE is real. The CGLE also exhibits spiral waves, so we can use established theory [31,33] to predict their wavelength λ,

$$\lambda = 2\pi\sqrt{\frac{D\left(1-\frac{\chi}{3+\sigma/\beta}\right)}{3(\mu_*-\mu)(1-|U|^2)}}, \tag{13}$$

where $|U|^2$ is the square of the amplitude of the solution of the CGLE, which only depends on ζ for fixed β and σ; see the Supplemental Material [46]. Equation (13) shows that the wavelength λ decreases for larger χ, and Figs. 3(b) and 3(c) show that the expression is close to our numerical estimates, even though μ is not very close to μ_*. Equation (13) also predicts that smaller mutation rates μ lead to shorter wavelengths, consistent with Fig. 3(c) and a previous study [25]. Interestingly, the length scale l_c^+ given in Eq. (12) also describes the observed behavior accurately; see Figs. 3(b) and 3(c). In fact, we find $\lim_{\mu\to\mu_*} l_c^+ = (1-|U|^2)^{1/2}\lambda$ close to the Hopf bifurcation. Finally, increasing the replacement rate ζ leads to smaller amplitudes $|U|$ and thus decreased wavelengths; see Fig. 3(b) and the Supplemental Material [46]. Note that we also observe patterns that are reminiscent of the Eckhaus and absolute instability of the CGLE [25,26] at large replacement rates ζ; see Fig. 4 in the Supplemental Material [46]. Taken together, we found that the mapping to the CGLE provides a faithful theoretical prediction of the length scales of spiral waves as a function of the relevant model parameters.

The dependence of the length scale λ of the spiral waves prompted us to hypothesize that spiral waves can only emerge when their intrinsic length scale is smaller than the system size. Indeed, the green dashed line in Fig. 2 indicates that spiral waves only emerge when $\lambda \lesssim L$. We thus conclude that the cases where we observe homogeneous oscillations would show spiral waves in larger systems.

We next quantify the frequency ω of the oscillating patterns using the first peak of the temporal correlation function $\tilde{g}_{AA}(t) = \tilde{g}_{AA}(|t_1 - t_2|) = \langle\phi_A(\mathbf{r}, t_1)\phi_A(\mathbf{r}, t_2)\rangle - \langle\phi_A(\mathbf{r}, t_1)\rangle\langle\phi_A(\mathbf{r}, t_2)\rangle$; see Fig. 3(d). Fig. 3 shows that the interaction parameter χ hardly affects ω in the weak-interaction regime ($\chi_A < \chi < \chi_R^*$). We rationalize this behavior by mapping Eq. (7) to a reaction-diffusion equation in the limit of weak interactions χ, revealing that χ only affects cross diffusion, but not the reactions; see the Supplemental Material [46]. The associated frequency ω_* of the most unstable mode is given by Eq. (5) and explains most of the behavior of the numerically determined ω. However, ω_* does not depend on the mutation rate μ, so this approximation cannot explain the dependence of ω on μ. To capture this phenomenologically, we use the mapping to the CGLE presented in the Supplemental Material [46], which provides a correction,

$$\omega = \omega_* - 3(\mu_* - \mu)c|U|^2, \tag{14}$$

where c is a constant depending on β, σ, and ζ; see Eq. (42) in the Supplemental Material [46]. This expression correctly predicts that ω is independent of χ and that it increases for larger ζ and μ; see Figs. 3(e) and 3(f).

Taken together, we find that weak repulsion in region WL shortens the wavelength of spiral waves, while their period is unaffected. A multiscale expansion around the Hopf bifurcation leads to a CGLE, which reveals that this behavior is caused by cross diffusion resulting from physical interactions, analogously to the effect of weak interactions on Turing patterns [34].

D. Oscillations and phase separation coexist for strong attractive interactions

We next focus on systems with strong attraction ($\chi < \chi_A$), where we first consider weak mutation rates ($\mu < \mu_*$, region AL). We expect that the spiral waves we found for weak attractions persist, albeit with longer wavelengths, following the observed trend in region WL. Indeed, Fig. 2 demonstrates spiral waves at low mutation rate (green circle), and Fig. 3 confirm that the length scale increases for smaller χ while the frequency stays almost constant. Moreover, the effects of the mutation rate μ and the replacement rate ζ are similar in regions WL and AL. However, we also observe that spiral waves form in a larger parameter region than expected: In region WL, boundary effects suppressed spiral waves that are comparable to or larger than the system size (white symbols above the green dashed line in Fig. 2), while this suppression is apparently much weaker in region AL. Since this transition coincides with the line $\chi = \chi_A$, we hypothesize that strong attractive interactions stabilize spiral waves.

Strong attraction can lead to phase separation, where the three species A, B, and C co-segregate from the solvent S. Indeed, the dark spots in the snapshots shown in Fig. 2(b) correspond to solvent-rich droplets, which are absent in region WL. Interestingly, these solvent droplets co-localize with defect cores of spiral waves. On the one hand, this suggests that phase separation can only proceed in the relatively calm defect cores while the comparatively strong spiral waves prevent phase separation by mixing the system effectively. Indeed, spatiotemporal chaos at large replacement rates ζ can prevent the formation of solvent droplets close to the transition ($\chi \lesssim \chi_A$); see Fig. 4 in the Supplemental Material [46]. On the other hand, the solvent droplets formed by phase separation apparently stabilize spiral waves, similar to rigid obstacles [3,49–51]. Taken together, positive feedback between formation of solvent droplets and spiral waves apparently stabilizes this state even if the system would otherwise be too small.

For larger mutation rates μ, spiral waves are absent even if $\mu < \mu_*$. Presumably, this is again caused by limitations imposed by the system size, consistent with the increasing pattern length scale shown in Fig. 3(c). When spiral waves are absent, phase separation can take place everywhere and we observe a regular hexagonal lattice of solvent droplets embedded in a phase enriched in the other species; see snapshot labeled by a white disk in Fig. 2. For stronger attraction, we also sometimes observe bicontinuous structures with a fixed length scale; see Fig. 2 in the Supplemental Material [46]. In both cases, coarsening is suppressed by reactions [52], and the correlation length scale l_{corr} is within the band of unstable real modes ($q_r^- < q < q_r^+$) predicted by the linear

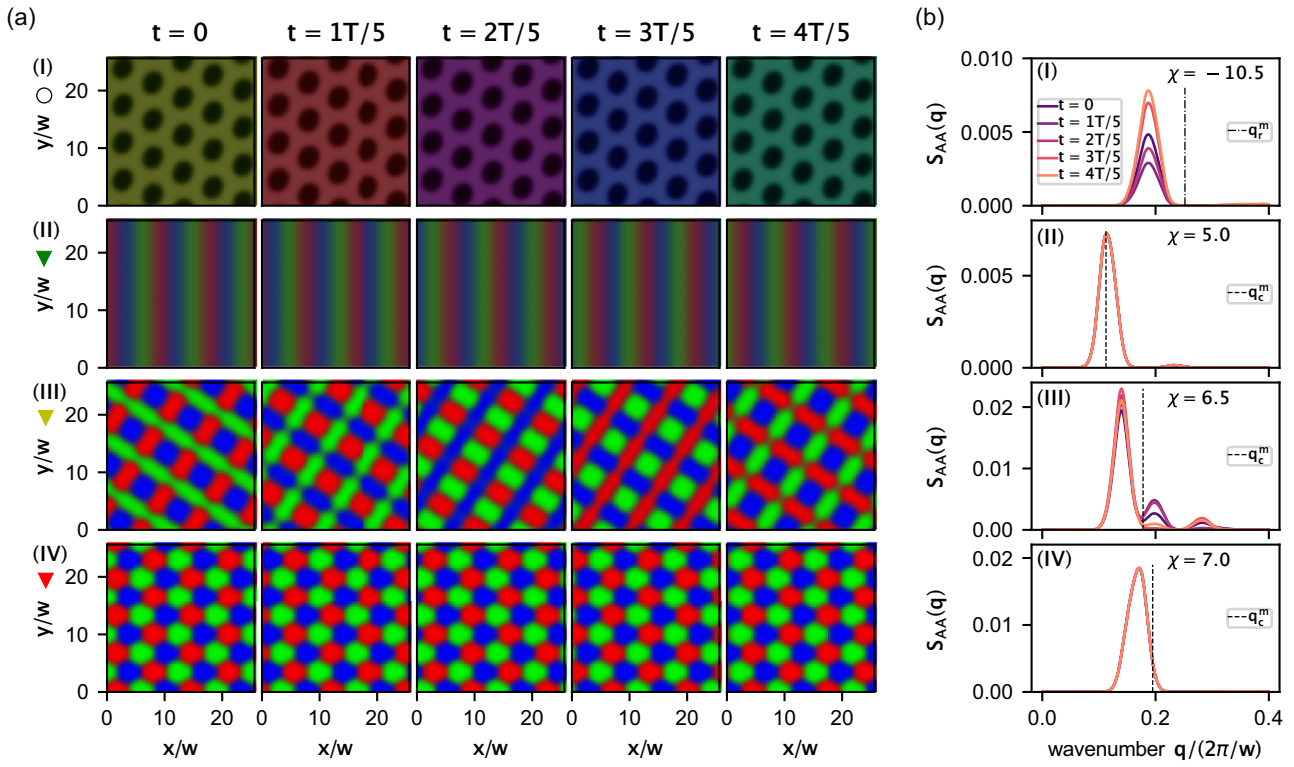

FIG. 4. Details of complex, oscillating patterns. (a) Snapshots showing one temporal period for four physical interactions ($\chi = -10.5, 5, 6.5, 7$; top to bottom) at $\mu = 0.05 > \mu_*$ and $\zeta = 1$. The corresponding periods are $T \approx 11\beta,\ 11\beta,\ 52\beta,\ 610\beta$. (b) Structure factors $S_{AA}(q)$ corresponding to data in panel (a). The vertical lines mark the wave number of the most unstable mode determined from linear stability analysis.

stability analysis; see the red symbols and green curves in Fig. 3(c). Moreover, Fig. 3(f) shows that the large connected phase oscillates between the three species A, B, and C with a frequency close to ω_*, consistent with the prediction of the frequency of the complex mode. Taken together, linear stability analysis predicts the most important properties of the hexagonally arranged solvent droplets embedded in an oscillating phase in region AL.

Linear stability analysis predicts that oscillations cease once the mutation rate μ becomes larger than μ_*. However, our numerical simulations of the full model show that the states do not change qualitatively when we cross this stability boundary: The hexagonal pattern of solvent droplets remains and the connected phase still oscillates between the three species; see Fig. 4(a)(I). While this behavior is obviously driven by nonlinear effects, the length scale of the hexagonal pattern still decreases for decreasing χ and increasing μ, consistent with the trend predicted by linear stability analysis.

We conclude that the competition of the Turing instability and the Hopf instability governs the behavior for strong attraction ($\chi < \chi_A$). For low μ and sufficiently large systems, we observe spiral waves with solvent droplets at their core, whereas hexagonal patterns of solvent droplets embedded in an oscillating phase emerge for larger μ and in small systems. Both behavior are impossible in excitable systems with ideal diffusion, demonstrating the qualitatively new effects that strong attraction between species can bring.

E. Strong repulsion leads to oscillating lattices

Finally, we discuss strong repulsion between species ($\chi > \chi_R$), where we predict a segregation of the species A, B, and C from each other while the solvent is homogeneously distributed. The linear stability analysis shown in Fig. 1 predicts that complex modes are unstable for all values of the mutation rate μ, whereas the critical value μ_* merely governs the stability of homogeneous perturbations ($q = 0$). Consequently, we expect oscillatory patterns in both the regions RH and RL.

Our numerical simulations shown in Fig. 4(a) reveal oscillating patterns for strong repulsion. For interaction strengths χ close to the critical value χ_R, the corresponding frequency ω is comparable to the value ω_* predicted by Eq. (5), but ω drops strongly with increasing repulsion χ; see Figs. 3(e) and 3(f). Concomitantly, the spatial patterns change: Close to the transition, we find oscillating stripes; see snapshots marked by green triangles in Figs. 2 and 4(a). As χ increases, the stripes first transition to slowly oscillating square lattices (marked by yellow triangles) and then further to slowly oscillating hexagonal lattices (marked by red triangles).

The length scales l_{corr} of these patterns are comparable to the length scales l_c^m of the most unstable mode, which also captures the observation that larger repulsion χ leads to smaller structures; see Figs. 3(a)–3(c). However, the observed increase of l_{corr} with decreasing μ and decreasing ζ cannot be explained by l_c^m and thus likely results from nonlinear effects. Moreover, for square and hexagonal lattices, l_{corr} is a bit larger than predicted from linear stability analysis, consistent with

results in reaction-diffusion systems [53]. Finally, the spatiotemporal chaos emerging at large replacement rates ζ can prevent the formation of regular patterns close to the transition ($\chi \gtrsim \chi_R$); see Fig. 4 in the Supplemental Material [46].

Taken together, this rich behavior indicates that strong repulsive interactions affect pattern formation strongly, presumably because repulsion segregates the species from each other so that the cyclic-dominant reactions are most active at interfaces.

III. DISCUSSION

We investigated the behavior of three species that interact physically and exhibit cyclic dominant reactions to study the effect of physical interaction on spatiotemporal patterns. For weak interactions, the mapping to the complex Ginzburg-Landau equation (CGLE) reveals that interactions mainly cause cross diffusion, which affects length scales but not time scales of the resulting spiral waves. In contrast, qualitatively new patterns emerge if interactions are strong: Strong attraction leads to phase separation of the solvent from all species, which exhibit spiral waves or oscillations. In this case, the typical coarsening of passive phase separation is suppressed, droplets can stabilize spiral waves, and oscillations appear even without a complex unstable mode in the linear stability analysis. Conversely, for strong repulsion, all species segregate from each other, limiting chemical interactions to interfaces, which results in various oscillating lattices. In summary, we find that linear stability analysis and the mapping to the CGLE explain the influence of weak interactions, whereas these approaches are less predictive for the qualitatively different patterns emerging for strong interactions.

Cyclic dominant reactions have been linked to biodiversity in ecological contexts [24,54], where the interplay of species and their respective survival impacts biodiversity. Our analysis suggests that repulsive interactions between species result in spatiotemporal patterns even for large mutation rates μ, where otherwise a single species would dominate. Conversely, attraction between species favors co-localization and the resulting competition makes extinction more likely. Moreover, physical interactions impact resulting dynamics qualitatively, suggesting that ecological patterns are affected and interactions need to be included when studying biodiversity.

We discussed a system where interesting spatial patterns emerge from the combination of two different pattern formation mechanisms. This is similar to active fluids, where reaction-diffusion processes and mechanochemical instabilities are simultaneously present [55]. Another example are droplets of the slime mold *Physarum polycephalum*, where the pattern frequency is controlled by reactions and diffusion of calcium, whereas the wavelength stems from the mechanochemical instability [56], analogously to our model with repulsive interactions. Similar combinations of multiple pattern-generating mechanisms will likely govern many biological processes to provide flexibility as well as robustness.

To build a general understanding of the impact of interactions in realistic systems, we will need to consider more complex models. For instance, we could consider more complex chemical reactions, e.g., including death rates [57] or nonsymmetric reactions [58], although some of the complexity might simply induce a renormalization of parameters [59]. In contrast, more diverse physical interactions can provide additional states already in equilibrium phase separation [38,60]. In particular, considering more than three species provides room for additional patterns [59,61,62], and we suspect that the lattices we observed at strong repulsion will look completely different. Realistic systems will also exhibit stochasticity [21] and spatial heterogeneity [22], which sometimes can be approximated by considering networks [63–65]. Finally, higher-order interactions might be frequent in nature and affect resulting patterns [66–68].

Beside these complex models, we also still lack basic understanding of (chemical) species that interact and react. Along these lines, it will be interesting to investigate thermodynamic constraints on spatiotemporal patterns. A recent paper already used linear stability analysis to investigate general nonideal reaction-diffusion systems [69], and this work needs to be extended to include oscillating patterns. It will be interesting to investigate fundamental physical constraints on creating spatiotemporal patterns, which will aid their reconstitution in experiments.

ACKNOWLEDGMENTS

C.L. thanks Lucas Menou for helping to set up the numerical calculations at the beginning of the project. We thank Yicheng Qiang for helpful discussions and critical reading of the paper. We also thank the two anonymous referees for helpful suggestions. Funding is gratefully acknowledged from the Max Planck Society and the European Union (ERC, EmulSim, 101044662).

[1] A. Zaikin and A. Zhabotinsky, Nature (London) **225**, 535 (1970).
[2] E. Palsson and E. C. Cox, Proc. Natl. Acad. Sci. USA **93**, 1151 (1996).
[3] J. M. Davidenko, A. V. Pertsov, R. Salomonsz, W. Baxter, and J. Jalife, Nature (London) **355**, 349 (1992).
[4] M. E. Hibbing, C. Fuqua, M. R. Parsek, and S. B. Peterson, Nat. Rev. Microbiol. **8**, 15 (2010).
[5] C. D. Nadell, K. Drescher, and K. R. Foster, Nat. Rev. Microbiol. **14**, 589 (2016).
[6] A. Corl, A. R. Davis, S. R. Kuchta, and B. Sinervo, Proc. Natl. Acad. Sci. USA **107**, 4254 (2010).
[7] D. Semmann, H.-J. Krambeck, and M. Milinski, Nature (London) **425**, 390 (2003).
[8] Z. Wang, B. Xu, and H.-J. Zhou, Sci. Rep. **4**, 5830 (2014).
[9] H. G. Michael Cross, *Pattern Formation and Dynamics in Nonequilibrium Systems*, 1st ed. (Cambridge University Press, Cambridge, 2009).
[10] M. E. Cates and J. Tailleur, Annu. Rev. Condens. Matter Phys. **6**, 219 (2015).

[11] M. Hildebrand, A. S. Mikhailov, and G. Ertl, Phys. Rev. Lett. **81**, 2602 (1998).
[12] M. Hildebrand, M. Kuperman, H. Wio, A. S. Mikhailov, and G. Ertl, Phys. Rev. Lett. **83**, 1475 (1999).
[13] Y. De Decker, H. Marbach, M. Hinz, S. Günther, M. Kiskinova, A. S. Mikhailov, and R. Imbihl, Phys. Rev. Lett. **92**, 198305 (2004).
[14] Y. De Decker and A. S. Mikhailov, J. Phys. Chem. B **108**, 14759 (2004).
[15] H. Marbach, S. Günther, T. Neubrand, and R. Imbihl, Chem. Phys. Lett. **395**, 64 (2004).
[16] K. John, S. Alonso, and M. Bär, Phys. Rev. E **90**, 052913 (2014).
[17] K. Kruse, Biophys. J. **82**, 618 (2002).
[18] G. Meacci and K. Kruse, Phys. Biol. **2**, 89 (2005).
[19] K. John and M. Bär, Phys. Biol. **2**, 123 (2005).
[20] H.-J. Zhou, Contemp. Phys. **57**, 151 (2016).
[21] A. Szolnoki, M. Mobilia, L.-L. Jiang, B. Szczesny, A. M. Rucklidge, and M. Perc, J. R. Soc., Interface **11**, 20140735 (2014).
[22] A. Szolnoki, B. De Oliveira, and D. Bazeia, Europhys. Lett. **131**, 68001 (2020).
[23] T. Reichenbach, M. Mobilia, and E. Frey, Phys. Rev. E **74**, 051907 (2006).
[24] T. Reichenbach, M. Mobilia, and E. Frey, Nature (London) **448**, 1046 (2007).
[25] B. Szczesny, M. Mobilia, and A. M. Rucklidge, Europhys. Lett. **102**, 28012 (2013).
[26] B. Szczesny, M. Mobilia, and A. M. Rucklidge, Phys. Rev. E **90**, 032704 (2014).
[27] M. Mobilia, A. M. Rucklidge, and B. Szczesny, Games **7**, 24 (2016).
[28] T. Nagatani and G. Ichinose, Complexity **2020**, 1 (2020).
[29] M. Mobilia, J. Theor. Biol. **264**, 1 (2010).
[30] E. Frey, Phys. A (Amsterdam, Neth.) **389**, 4265 (2010).
[31] I. S. Aranson and L. Kramer, Rev. Mod. Phys. **74**, 99 (2002).
[32] M. Van Hecke, C. Storm, and W. van Saarloos, Phys. D (Amsterdam, Neth.) **134**, 1 (1999).
[33] I. S. Aranson, L. Kramer, and A. Weber, Phys. Rev. E **47**, 3231 (1993).
[34] L. Menou, C. Luo, and D. Zwicker, J. R. Soc., Interface **20**, 20230244 (2023).
[35] S. Safran, *Statistical Thermodynamics of Surfaces, Interfaces, and Membranes* (CRC Press, 2018).
[36] M. Rubinstein, R. H. Colby *et al.*, *Polymer Physics* (Oxford University Press, New York, 2003), Vol. 23.
[37] J. W. Cahn and J. E. Hilliard, J. Chem. Phys. **28**, 258 (1958).
[38] S. Mao, D. Kuldinow, M. Haataja, and A. Košmrlj, Soft Matter **15**, 1297 (2019).
[39] D. Zwicker, Curr. Opin. Colloid Interface Sci. **61**, 101606 (2022).
[40] J. F. Nash Jr, Proc. Natl. Acad. Sci. USA **36**, 48 (1950).
[41] R. M. May and W. J. Leonard, SIAM J. Appl. Math. **29**, 243 (1975).
[42] B. Szczesny, *Coevolutionary Dynamics in Structured Populations of Three Species* (University of Leeds, 2014).
[43] F. Jülicher, S. W. Grill, and G. Salbreux, Rep. Prog. Phys. **81**, 076601 (2018).
[44] S. de Groot and P. Mazur, *Non-Equilibrium Thermodynamics*, Dover Books on Physics (Dover Publications, 1984).
[45] E. J. Kramer, P. Green, and C. J. Palmstrøm, Polymer **25**, 473 (1984).
[46] See Supplemental Material at http://link.aps.org/supplemental/10.1103/PhysRevE.108.034206 for details on the linear stability analysis of the model, multiscale expansion to CGLE, and additional simulation snapshots and movies, which includes Refs. [9,25,26,34,42].
[47] N. Ziethen, J. Kirschbaum, and D. Zwicker, Phys. Rev. Lett. **130**, 248201 (2023).
[48] D. Zwicker, J. Open Source Software **5**, 2158 (2020).
[49] T. F. Eckstein, E. Vidal-Henriquez, A. J. Bae, and A. Gholami, Sci. Signal. **13**, eaaz3975 (2020).
[50] V. S. Zykov, Philos. Trans. R. Soc., A **376**, 20170379 (2018).
[51] A. M. Pertsov, J. M. Davidenko, R. Salomonsz, W. T. Baxter, and J. Jalife, Circ. Res. **72**, 631 (1993).
[52] D. Zwicker, A. A. Hyman, and F. Jülicher, Phys. Rev. E **92**, 012317 (2015).
[53] L. Yang, A. M. Zhabotinsky, and I. R. Epstein, Phys. Rev. Lett. **92**, 198303 (2004).
[54] D. Tilman, Ecology **75**, 2 (1994).
[55] J. S. Bois, F. Jülicher, and S. W. Grill, Biophys. J. **100**, 445a (2011).
[56] M. Radszuweit, H. Engel, and M. Bär, PLoS One **9**, e99220 (2014).
[57] S. Islam, A. Mondal, M. Mobilia, S. Bhattacharyya, and C. Hens, Phys. Rev. E **105**, 014215 (2022).
[58] M. Berr, T. Reichenbach, M. Schottenloher, and E. Frey, Phys. Rev. Lett. **102**, 048102 (2009).
[59] M. Peltomäki and M. Alava, Phys. Rev. E **78**, 031906 (2008).
[60] D. Zwicker and L. Laan, Proc. Natl. Acad. Sci. USA **119**, e2201250119 (2022).
[61] A. Bayliss, A. Nepomnyashchy, and V. Volpert, Phys. D (Amsterdam, Neth.) **411**, 132585 (2020).
[62] J. Hu, D. R. Amor, M. Barbier, G. Bunin, and J. Gore, Science **378**, 85 (2022).
[63] C. M. Postlethwaite and A. M. Rucklidge, Nonlinearity **35**, 1702 (2022).
[64] A. Szolnoki and G. Szabó, Phys. Rev. E **70**, 037102 (2004).
[65] P. M. Geiger, J. Knebel, and E. Frey, Phys. Rev. E **98**, 062316 (2018).
[66] F. Palombi, S. Ferriani, and S. Toti, Eur. Phys. J. B **93**, 194 (2020).
[67] T. Gibbs, S. A. Levin, and J. M. Levine, Proc. Natl. Acad. Sci. USA **119**, e2205063119 (2022).
[68] C. Griffin and R. Wu, arXiv:2301.02518.
[69] T. Aslyamov, F. Avanzini, É. Fodor, and M. Esposito, arXiv:2304.06394 (2023).